

Joint Visible Light and Backscatter Communications for Proximity-Based Indoor Asset Tracking Enabled by Energy-Neutral Devices

Boxuan Xie, *Graduate Student Member, IEEE*, Lauri Mela, Alexis A. Dowhuszko, *Senior Member, IEEE*,

Yu Bai, *Graduate Student Member, IEEE*, Zehui Xiong, *Senior Member, IEEE*,

Zhu Han, *Fellow, IEEE*, Dusit Niyato, *Fellow, IEEE*, and Riku Jäntti, *Senior Member, IEEE*

Abstract—In next-generation wireless systems, providing location-based mobile computing services for energy-neutral devices has become a crucial objective for the provision of sustainable Internet of Things (IoT). Visible light positioning (VLP) has gained great research attention as a complementary method to radio frequency (RF) solutions since it can leverage ubiquitous lighting infrastructure. However, conventional VLP receivers often rely on photodetectors or cameras that are power-hungry, complex, and expensive. To address this challenge, we propose a hybrid indoor asset tracking system that integrates visible light communication (VLC) and backscatter communication (BC) within a simultaneous lightwave information and power transfer (SLIPT) framework. We design a low-complexity and energy-neutral IoT node, namely backscatter device (BD) which harvests energy from light-emitting diode (LED) access points, and then modulates and reflects ambient RF carriers to indicate its location within particular VLC cells. We present a multi-cell VLC deployment with frequency division multiplexing (FDM) method that mitigates interference among LED access points by assigning them distinct frequency pairs based on a four-color map scheduling principle. We develop a lightweight particle filter (PF) tracking algorithm at an edge RF reader, where the fusion of proximity reports and the received backscatter signal strength are employed to track the BD. Experimental results show that this approach achieves the positioning error of 0.318 m at 50th percentile and 0.634 m at 90th percentile, while avoiding the use of complex photodetectors and active RF synthesizing components at the energy-neutral IoT node. By demonstrating robust performance in multiple indoor trajectories, the proposed solution enables scalable, cost-effective, and energy-neutral indoor tracking for pervasive and edge-assisted IoT applications.

Index Terms—Ambient IoT, backscatter communication, visible light communication, indoor positioning, asset tracking.

I. INTRODUCTION

IN the emerging sixth-generation (6G) era, growing demand for energy-efficient and cost-effective Internet of Things (IoT) devices aligns with future network key impact

B. Xie, L. Mela, A. Dowhuszko, Y. Bai, and R. Jäntti are with the Department of Information and Communications Engineering, Aalto University, 02150 Espoo, Finland (e-mail: boxuan.xie@aalto.fi, lauri.mela@aalto.fi, alexis.dowhuszko@aalto.fi, yu.bai@aalto.fi, riku.jantti@aalto.fi)

Z. Xiong is with the School of Electronics, Electrical Engineering and Computer Science (EEECS), Queen's University Belfast, Belfast, BT7 1NN, U.K. (z.xiong@qub.ac.uk).

Z. Han is with the Department of Electrical and Computer Engineering, University of Houston, Houston, TX 77004 USA, and also with the Department of Computer Science and Engineering, Kyung Hee University, Seoul 446-701, South Korea (email: hanzhu22@gmail.com).

D. Niyato is with the College of Computing and Data Science, Nanyang Technological University, Singapore 639798 (email: dniyato@ntu.edu.sg).

Manuscript received ; revised .

factors (KPIs) of reduced power consumption and complexity [1], [2]. Meanwhile, many IoT devices require accurate indoor positioning service, especially for application scenarios such as logistics, healthcare, and industrial automation. These services rely on seamless localization and tracking of IoT devices, which is challenging due to multipath-rich indoor environments [3]. A recent proposal within the third generation partnership project (3GPP), referred to as Ambient IoT [4], highlights energy-neutral IoT nodes with built-in positioning functionalities, drawing further attention to low-power, low-cost, and high-accuracy indoor positioning methods [5]. This increasing interest underlines the significance of exploring new solutions that integrate efficient energy harvesting and localization capabilities for IoT devices.

Global Navigation Satellite Systems (GNSSs) offer reliable positioning in outdoor areas [6], yet the positioning accuracy degrades inside buildings due to severe signal attenuation and multipath fading. As a result, a variety of radio frequency (RF) technologies, including WiFi [7], Bluetooth [8], LoRa [9], cellular networks [10], radio frequency identification (RFID) [11], and ultra-wide-band (UWB) [12], have been investigated for indoor positioning. These systems exploit measurements of received signal strength (RSS), time of arrival (ToA), time difference of arrival (TDoA), or angle of arrival (AoA), which can be augmented by multi-antenna techniques to improve the positioning accuracy. However, the inherent trade-offs between positioning precision, hardware complexity, and deployment cost continue to pose a significant challenge for practical IoT implementations with low-complexity requirement.

The broad adoption of light-emitting diodes (LEDs) has attracted the attention on the use of visible light communication (VLC), enabling luminaires to transmit information over optical wireless links [13]. VLC offers a promising pathway for indoor localization, typically referred to as visible light positioning (VLP) [14]–[16]. Previous works by Zhu *et al.* [15] and Bastiaens *et al.* [16] have presented comprehensive overviews of fundamentals and system designs of VLP systems. Studies of Yang *et al.* [17]–[19] employed measurements of VLC signals including RSS-, phase-, and time-based approaches to accommodate various positioning accuracy requirements. They have also investigated resource allocation to provide different quality-of-service (QoS) in VLP systems [19], [20], aiming at ensuring stable indoor communication and positioning for IoT nodes. Despite these advances, VLC receivers in such systems often rely on specialized photodetectors or camera sensors and incorporate

energy-intensive components, such as transimpedance amplifiers (TIAs), resulting in increased power consumption and hardware complexity, which in turn adds to the overall cost on the IoT device side. Therefore, designing low-power and low-complexity VLP solutions still remains a key challenge for cost-effective IoT deployment.

Among VLP technologies, proximity-based positioning is one simple method to localize IoT devices under indoor illumination, as the location of the IoT device is approximated by the known position of the nearest VLC access points (APs) [21]–[23]. Although these proximity-based approaches suit many low-data-rate scenarios, they assume that the IoT device performs both VLC reception and location estimation. This dual role is less practical for asset tracking, where position reports are usually collected and monitored by a distant edge reader. Moreover, conventional VLC receivers rely on specialized hardware in transmission and reception that limits their applicability in resource-limited and energy-constrained IoT devices. Therefore, there is a need for an energy-efficient and low-complexity VLC-based and proximity-reporting method at the IoT device to enable scalable indoor IoT asset tracking.

Recently, hybrid VLC/RF networks have emerged as a promising strategy to take advantage of high data rates from collocated VLC and ubiquitous coverage from RF systems [24], [25]. Early studies focused on IoT devices equipped with both VLC receivers and active RF transmitters to relay VLC data to conventional RF receivers [26], [27]. Alongside these relay-based approaches, simultaneous lightwave information and power transfer (SLIPT) has gained momentum as a technique to energize IoT devices via LED illumination while delivering data [28], [29]. For instance, Peng *et al.* considered optimizing end-to-end performance of the IoT relay-enabled hybrid VLC/RF system under transmission power constraints [27], and Tang *et al.* studied different sustainability-driven resource allocation for hybrid VLC/RF systems [30]. Although these research works have shown the potential to achieve lower operating costs and improved energy efficiency, they generally assume active RF transmitters on the IoT nodes, which increases device complexity.

To address the challenge of proximity report through RF channels by using active RF components, recent advances in ambient backscatter communication (BC) open an alternative promising route, which allows ultra-low-power RF transmissions by modulating existing RF signals without the need of energy-intensive local oscillators and power amplifiers in the IoT devices [31]–[33]. In this regard, communications schemes integrating VLC with BC in hybrid VLC/RF networks have been explored in [34]–[38]. Among these works, Giustiniano *et al.* introduced a system named BackVLC that employs LED bulbs for both illumination and data transmission [34], enabling battery-free IoT tags to communicate using visible light and RF backscatter signals. Similarly, Mir *et al.* proposed TunnelLiFi [35], an IoT node that bridges visible light and radio spectrum using a tunnel diode oscillator for low-power conversion, enabling the relaying of LiFi signals to other IoT devices. They also developed PassiveLiFi [36], a system integrating VLC with RF backscatter communications, which uses a chirp spread spectrum VLC transmitter to improve

the communication range and efficiency. Xie *et al.* explored LiBD [37], a backscatter device (BD) that uses visible light for both control and power purposes in BC over sub-6 GHz bands. They also designed a thin film BD fabricated through inkjet printing and additive manufacturing on flexible substrates [38], converting light-carrying data into RF signals and performing under different lighting conditions. Koskinen *et al.* developed Li2BC [39], a BD that integrates functionalities of VLC receiving and processing, as well as backscatter modulation, leveraging a low-power microcontroller.

Despite these developments, a unified, energy-neutral solution for indoor positioning that combines VLC with RF backscatter at IoT devices remains an open challenge. In this paper, we propose a comprehensive joint VLC-BC-enabled indoor asset tracking system. The design features a multi-cell, frequency division multiplexing (FDM)-based VLC transmission architecture where multiple LED luminaires illuminate the service area and broadcast location-specific identifiers (IDs) to a BD as its proximity information. We design a low-complexity, battery-free BD that harvests energy from the VLC signals and then modulates and backscatters ambient RF carrier waves to report proximity to an edge reader. The reader executes a tracking algorithm to estimate the position of the BD. The key contributions of this paper are listed as follows:

- We propose an indoor asset tracking system that integrates VLC and BC under a SLIPT framework. The design leverages on a batteryless IoT node, namely BD, as a light-to-RF relay for delivering proximity information to an RF reader at the edge for location inference. This approach enables low hardware complexity at the IoT node, as the BD can harvest energy from LED illumination and backscatter existing RF signals without the requirement of active radio synthesizing components.
- We design a multi-cell VLC architecture based on FDM method to address light interference among multiple LED APs. Each LED AP embeds a unique ID using the binary frequency-shift keying (BFSK) to modulate the intensity of emitted optical signals. The low-complexity light modulation and multiplexing scheme offers a scalable solution for identifying which VLC cell that the BD is located, thereby enabling simple proximity-based positioning.
- We develop a novel algorithm employing a particle filter (PF) to track the BD in real time at an edge RF reader. By fusing two kinds of measurements, namely the proximity reports indicating the nearest VLC cell IDs and the RSS of the backscatter signal, the designed algorithm can estimate the position of the BD. This approach effectively addresses the uncertainty in measurement noise and offers robustness against multipath-rich indoor environments.
- We present a proof of concept of the proposed system, demonstrating communications among LED luminaires, a BD, an RF source (RFS), and a reader. The BD harvests energy and receives LED IDs over VLC links, and utilizes the backscatter link for proximity report to the reader. Through both simulations and measurements with multiple movement trajectories of the BD, we show that the proposed system achieves submeter-level tracking

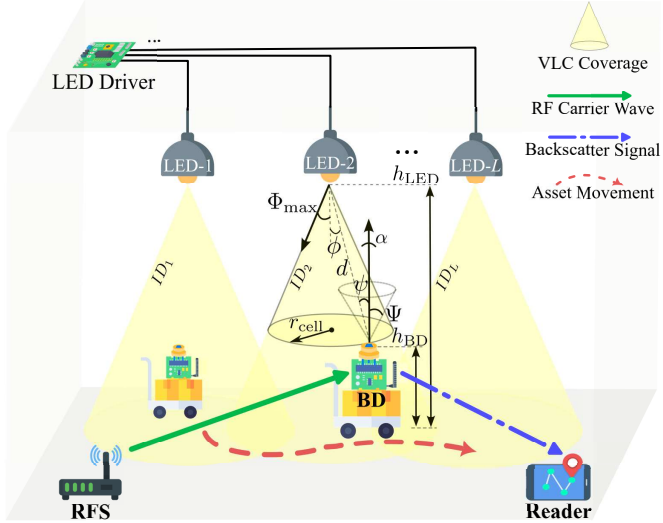


Fig. 1. Overview of the joint VLC-BC system proposed for indoor asset tracking. The BD attached to the asset receives LED IDs over light (yellow cones) and convert it to electrical signal to modulate the ambient RF carrier waves (green arrow) emitted by the RFS. The modulated signal is backscattered (blue arrow) and detected by an edge reader for location inference.

accuracy, highlighting practical energy-neutral and low-complexity operation for asset tracking applications.

The rest of the paper is organized as follows. Section II introduces the joint VLC-BC system model. Section III describes the tracking task, presents the details of the multi-cell VLC deployment, and describes the PF-based tracking algorithm design. Section IV illustrates the implementation of the proposed system with end-to-end communication modules. Then, Section V presents and evaluates the simulation and experimental results. Finally, Section VI draws conclusions.

II. SYSTEM MODEL

The proposed joint VLC-BC system for indoor asset tracking is depicted in Fig. 1. In this scenario, the position of a target asset moving across the floor is tracked with the aid of an edge reader. An IoT node, namely a BD, is attached directly to the asset. Multiple LED APs illuminate the service area and continuously broadcast their unique IDs through VLC. Each of these ID can be mapped to the known location of an LED AP in a database. When the BD moves into the coverage area of an LED AP, it receives the ID of the LED AP from the VLC link, and the BD forwards that ID to the distant reader by modulating and backscattering ambient RF carriers emitted by an RFS over the BC link. Finally, the reader captures the backscattered signal and detects the IDs matched to the LED APs, such that the reader can estimate the position of the BD.

The detailed schematic diagram of the system is presented in Fig. 2. LED APs transmit VLC signals to the BD using an intensity modulation/direct detection (IM/DD) scheme, and the message is received by the BD when being within the coverage range of the LED APs. The BD in this setup consists of a photodetector, an energy harvester, a backscatter modulator, and an RF antenna [37], [38]. Since the LED APs are designed to transmit their IDs with low data rate, in the order of few kbps,

this paper considers the use of photovoltaic (PV) cells as the photodetector. The alternating current/direct current (AC/DC) splitter separates the photovoltaic-converted signals into electrical AC and DC components. The AC component, which carries the VLC message, is used to control the backscatter modulation. On the other hand, the DC component supplies energy to the BD. Then, the BD modulates the captured ambient RF carrier waves coming from the RFS, which can typically be, e.g., a WLAN AP. The AC component controls the modulation of the amplitude of the RF carrier waves, which generates the required alternation of the reflection coefficients of the BD. The modulated signal is then backscattered and captured by the reader equipped with conventional RF front ends. The reader decodes the signal including the proximity information of the BD, and measure the RSS of the received signal. These two measurements are combined by a tracking algorithm to localize and track the position of the BD. In the following sections, the VLC and BC links used in this paper are briefly presented.

A. VLC Channel Model

In the downlink direction of the VLC transmission, each LED AP is assigned with a unique ID and transmits its individual VLC signal using frequency-division multiplexing (FDM) method. Binary frequency-shift keying (BFSK) baseband modulation is used to generate the square-wave AC current that modulates the intensity of the light emitted by the LED, while a bias-tee is employed to add a DC bias to the modulating signal. Let $m(t)$ denote the LED-modulating AC signal at time t , which can be expressed by

$$m(t) = \begin{cases} \text{sgn}(\sin(2\pi f_1 t)), & \text{bit} = 0, \\ \text{sgn}(\sin(2\pi f_2 t)), & \text{bit} = 1, \end{cases} \quad (1)$$

where $\text{sgn}(\cdot)$ denotes the sign function, f_1 and f_2 represent the modulating frequencies of the BFSK scheme. Let $l = 1, \dots, L$ represent the indices of LED APs. Then, the electrical signal that drives the l -th LED AP can be written as $s_l(t) = m_l(t) + I_B$, where I_B represents the DC biasing current driving the LED. Therefore, the transmitted optical signal can be expressed by [28]

$$P_l^{\text{LED}}(t) = \eta_{\text{E-O}}(m_l(t) + I_B), \quad (2)$$

where $\eta_{\text{E-O}}$ is the LED electric-to-optical power conversion factor. Since a practical LED transmitter operates within a limited linear region, the peak amplitude s_{\max} of $s_l(t)$ should be bounded to avoid clipping. Specifically, $s_{\max} \leq \min(I_B - I_{\min}, I_{\max} - I_B)$, where I_{\max} and I_{\min} denote the maximum and minimum driving current, respectively.

To characterize the VLC channel, a direct illumination model is adopted as shown in Fig. 1, based on the assumption that the direct optical signal is significantly stronger than any reflected signals [40]. Phosphor-coated LEDs are considered and assumed to emit light following a Lambertian radiation pattern. Within its coverage area, each LED AP maintains a line-of-sight (LoS) link to the BD. For simplicity, in this paper we assume that the BD and its photodetector share the same position, with a prototype shown in Fig. 5. Then, the DC

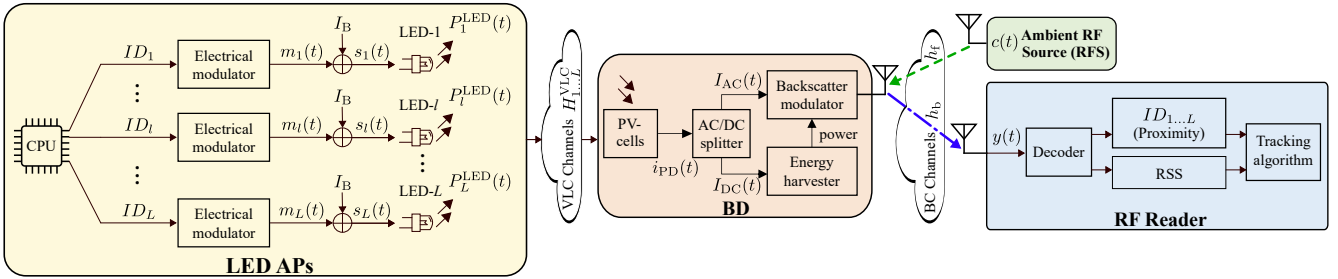


Fig. 2. A schematic diagram of the joint VLC-BC system. LED APs illuminate the indoor space and transmit unique IDs through VLC links. The BD receives VLC signals and converts them into electrical signals, whose DC components are used to power the BD while AC components are used to modulate the captured RF carriers emitted by the RFS. The modulated signal is backscattered toward the RF reader, which is decoded and used for positioning purposes.

gain of the optical channel between LED- l and BD-equipped photodetector can be written as [40]

$$H_l^{\text{VLC}} = \begin{cases} \frac{(\nu+1)A_{\text{PD}}}{2\pi d_l^2} \cos^\nu(\phi_l) \cos(\psi_l), & |\psi_l| \leq \Psi, \\ 0, & |\psi_l| > \Psi, \end{cases} \quad (3)$$

where d_l denotes the Euclidean distance between LED- l and the BD, and $\nu = -1/\log_2[\cos(\Phi_{\text{max}})]$ refers to the Lambertian index of the LEDs. The parameter Φ_{max} indicates the semi-angle at half-power of the LED, where Ψ defines the field-of-view (FoV) semi-angle of the photodetector with an active area of A_{PD} . Furthermore, $\phi_l \geq 0$ and ψ_l are the irradiance and incidence angles of the LoS link between LED- l and the BD, respectively. The orientation of the BD, which is given by $\alpha_l = \phi_l - \psi_l$, represents the angular deviation of the direction where the axis of the acceptance cone of the photodetector is pointing with respect to the upward direction.

The aggregated VLC signal power that arrives at the BD can be expressed by $\sum_{l=1}^L P_l^{\text{LED}} H_l^{\text{VLC}}$, where L is the total number of LED APs. Therefore, the BD-equipped photodetector outputs electrical current, given as

$$\begin{aligned} i_{\text{PD}}(t) &= \eta_{\text{O-E}} (\sum_{l=1}^L P_l^{\text{LED}} H_l^{\text{VLC}}) + n(t) \\ &= I_{\text{AC}}(t) + I_{\text{DC}}(t) + n(t), \end{aligned} \quad (4)$$

where $\eta_{\text{O-E}}$ is the optical-to-electrical responsivity of the photodetector, $I_{\text{AC}}(t)$ and $I_{\text{DC}}(t)$ are the AC and DC components of the received optical signal, respectively, and $n(t)$ is additive white Gaussian noise with variance $N_0 B$, with N_0 being the noise power spectral density and B the system operational bandwidth. Furthermore, the output AC component carrying the VLC message attains the form given by

$$I_{\text{AC}}(t) = \eta_{\text{O-E}} \sum_{l=1}^L \eta_{\text{E-O}} H_l^{\text{VLC}} m_l(t). \quad (5)$$

Furthermore, to supply the energy that is needed to power up the BD circuitry, such as the backscatter modulator, energy harvesting is performed using the DC component $I_{\text{DC}}(t)$ output from the BD-equipped photodetector. The amount of energy that can be harvested upon reception of the VLC signal can be written as [26]

$$E_h = \varepsilon I_{\text{DC}} V_{\text{OC}} = \varepsilon \eta_{\text{O-E}} (\sum_{l=1}^L \eta_{\text{E-O}} H_l^{\text{VLC}} I_{\text{B}}) V_{\text{OC}}, \quad (6)$$

where ε is the fill factor of the photodetector, V_{OC} is the open circuit voltage given by

$$V_{\text{OC}} = V_t \ln \left(1 + \frac{\eta_{\text{O-E}} (\sum_{l=1}^L \eta_{\text{E-O}} H_l^{\text{VLC}} I_{\text{B}})}{I_0} \right), \quad (7)$$

where V_t is the thermal voltage and I_0 is the dark saturation current of the BD-equipped photodetector.

B. Backscatter Channel Model

The BC link comprises an RFS, a BD, and an RF reader. The BD modulates the carrier signals emitted by the RFS using photovoltaic-converted VLC signals and subsequently backscatters the modulated signals to the reader. The received backscatter signal at the reader is then expressed by [41]

$$y(t) = \sqrt{\xi G_{\text{T}} G_{\text{R}} G_{\text{BD}}} h_f(t) h_b(t) c(t) I_{\text{AC}}(t) + n(t), \quad (8)$$

where ξ denotes the backscatter efficiency of the BD, and G_{T} , G_{R} , and G_{BD} are the antenna gains of the RFS, reader, and BD, respectively. The symbol h_f is the forward channel gain (RFS \rightarrow BD) between the RFS and the BD, and h_b is the backscatter channel gain (BD \rightarrow reader) between the BD and reader, respectively. The ambient RF carrier signal $c(t)$ coming from the RFS has a mean power of $P_c = \mathbb{E}\{|c(t)|^2\}$. Furthermore, $I_{\text{AC}}(t)$ represents the AC component of photovoltaic-converted VLC signal presented in (5) and is used to modulate with the RF carrier signal. The term $n(t)$ is the additive white Gaussian noise with variance $N_0 B$. Moreover, ξ is related to the polarization mismatch χ_f between the RFS and BD, and χ_b models the mismatch between the BD and reader. Finally, the modulation factor of the BD is given by M , and Θ represents an object penalty; thus, the backscatter efficiency can be expressed by $\xi = (\chi_f \chi_b M) / \Theta^2$ [41]. For practical reasons, the radio channels h_f and h_b is modeled using the 3GPP Indoor Hotspot model [42]. The model defines path losses for LoS and non-line-of-sight (NLoS) conditions, expressed by

$$\mathcal{L}_{\text{LoS},\text{dB}} = 32.4 + 17.3 \log_{10}(d_{3D}) + 20 \log_{10}(f_c) + \delta_{\text{LoS},\text{dB}}, \quad (9)$$

$$\begin{aligned} \mathcal{L}_{\text{NLoS},\text{dB}} &= \max(\mathcal{L}_{\text{LoS},\text{dB}}, 17.3 + 38.3 \log_{10}(d_{3D}) \\ &\quad + 24.9 \log_{10}(f_c) + \delta_{\text{NLoS},\text{dB}}), \end{aligned} \quad (10)$$

where d_{3D} represents the 3D Euclidean distance between a transmitter and a receiver, f_c is the carrier frequency in gigahertz, and $\delta_{\text{LoS},\text{dB}}$ is the shadowing factor modeled as a lognormal random variable with $\sigma_{\text{LoS}} = 3$ dB for $1 \leq d_{3D} \leq 150$ m. Similarly, $\delta_{\text{NLoS},\text{dB}}$ is the shadowing factor modeled as a lognormal random variable with $\sigma_{\text{NLoS}} = 8.03$ dB for $1 \leq d_{3D} \leq 150$ m. The probability of having an LoS link varies with the target kind of environment.

In an open indoor environment, the LoS probability is given by [42]

$$\text{Pr}_{\text{LoS}} = \begin{cases} 1, & d_{2D} \leq 5 \text{ m}, \\ e^{-\frac{d_{2D}-5}{70.8}}, & 5 < d_{2D} \leq 49 \text{ m}, \\ 0.54e^{-\frac{d_{2D}-49}{211.7}}, & d_{2D} > 49 \text{ m}, \end{cases} \quad (11)$$

where d_{2D} is the horizontal distance between the transmitter and receiver. Finally, the expected value of the overall path loss at a given distance, which combines the LoS and NLoS conditions weighted by their respective probabilities, can be written as

$$\mathcal{L}_{\text{dB}} = \text{Pr}_{\text{LoS}} \mathcal{L}_{\text{LoS,dB}} + (1 - \text{Pr}_{\text{LoS}}) \mathcal{L}_{\text{NLoS,dB}}. \quad (12)$$

Hence, the RSS of the received backscatter signal can be expressed by

$$R^{\text{BC}} = \xi G_{\text{R}} G_{\text{BD}}^2 I_{\text{AC}}^2 P_{\text{c}} \mathcal{L}_{\text{f}}^{-1} \mathcal{L}_{\text{b}}^{-1}, \quad (13)$$

where $\mathcal{L}_{\text{f}} = |h_{\text{f}}|^{-2}$ and $\mathcal{L}_{\text{b}} = |h_{\text{b}}|^{-2}$ represent the path losses of forward channel and backscatter channel, respectively.

III. PROXIMITY-BASED ASSET TRACKING

This section describes the task of tracking the BD in an indoor environment based on the proximity information coming from LED APs and on the RSS of backscatter signals. We first present the underlying challenges and detail the tracking task in a state-space framework in Section III-A. We then describe the VLC cell model in Section III-B, where each LED AP provides coverage in a limited region, and explain how the FDM-based approach enables the reception of multiple overlapping light signals in Section III-C. Finally, we develop a lightweight particle filtering-based algorithm to fuse the proximity information of the BD and the RSS of the backscatter signal for tracking purpose in Section III-D.

A. Task Description

Consider a set of ceiling-mounted LED APs illuminating an indoor environment. As the BD moves across this service area, it detects the unique IDs of any nearby LED APs that is in coverage range. These IDs are then forwarded to a distant RF reader using the backscatter communication mechanism. Consequently, the proximity of the BD to a particular LED AP, or sets of APs with overlapping coverage regions, is reported whenever the BD is illuminated by one or more APs. If the BD is outside all of the VLC coverage areas, it does not receive and forward any ID. By decoding and analyzing the backscattered signal, the reader can estimate the position of the BD. To interpret the above mechanism into a tracking problem, we identify three pivotal issues. First, we need an accurate representation of the coverage region of an LED AP, also known as VLC cell service area, to determine whether the BD is within the coverage range of the cell. Second, when moving into overlapping regions of VLC cells, the BD will likely detect multiple VLC signals and multiple LED IDs simultaneously, thus requiring a robust multiplexing method to differentiate them. Third, we need to develop a tracking algorithm at the reader that incorporates two measurements:

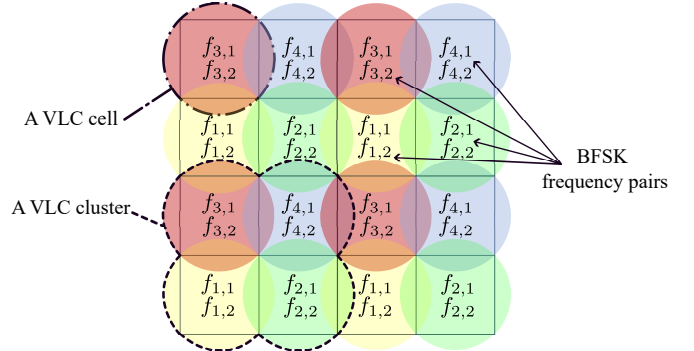


Fig. 3. An example of VLC deployment based on FDM. A VLC cluster consists of four VLC cells denoted by four different colors. Within a cluster, each cell adopts a distinct frequency pair to implement the BFSK modulation to transmit the VLC cell ID, avoiding interference between adjacent cells.

- (i) the set of LED IDs detected and forwarded by the BD, and
- (ii) the RSS of the backscatter signal, to localize and track the BD over time.

B. VLC Cell Model

The coverage area of each LED AP can be approximated as a circle on the light-receiving plane parallel to the floor, known as a VLC cell service area [40]. This approximation is determined by the LoS geometry between the LED AP and the BD-equipped photodetector. As illustrated in Fig. 1, let h_{LED} and h_{BD} denote the vertical positions of ceiling-mounted LED AP and the height of BD to the floor, respectively. Suppose the BD is oriented toward the ceiling with an FoV semi-angle Ψ . Then, the nominal radius of the VLC cell is expressed by [40]

$$r_{\text{cell}} = (h_{\text{LED}} - h_{\text{BD}}) \tan(\Psi). \quad (14)$$

When the horizontal distance of the BD to an LED AP does not exceed r_{cell} , the reception of the VLC signal can be guaranteed if the VLC link is dimensioned accordingly. If the BD moves outside the VLC cell radius, the VLC link will be disrupted as shown in (3). This geometric relation also depends on rotation or tilting of the BD [40], [43]; yet for simplicity, this paper considers an upward orientation of the BD.

C. Deployment of the Multi-Cell VLC System

In the proposed system, capturing VLC data from multiple LED APs concurrently necessitates a multiplexing scheme to distinguish their transmissions. One option is time-division multiplexing (TDM), where each LED AP transmits in a specific time slot while remaining idle at other times [22]. However, TDM-based approaches impose strict synchronization requirements and potentially large positioning delays if the number of LED APs is high. To avoid these drawbacks, this paper proposes the use of an FDM-based scheme that allocates each LED AP a unique BFSK frequency pair for data transmission, as shown in Fig. 3. This design is inspired by the classic four-color theorem in graph theory [44], [45], which implies that a sufficient number of frequency pairs can be allocated such that adjacent VLC cells do not share the same pair to avoid strong co-channel interference. Since each LED AP transmits with a unique frequency signature, the BD

can simultaneously receives multiple BFSK-modulated VLC signals from all the LED APs whose cells cover its position.

Fig. 3 presents an example, where each cluster of four LED APs adopts four distinct BFSK frequency pairs. By examining which frequency components appear in the backscattered signal coming from the BD, the RF reader can determine which LED APs illuminate the current position of the BD. As a result, proximity information can be received and forwarded by the BD without significant delay or tight synchronization requirements.

D. Particle Filter-Based Tracking Algorithm Design

This subsection proposes a novel tracking algorithm for the fusion of reader-decoded LED IDs and RSS measurements of backscatter signals. The objective is to iteratively estimate the position of the BD under uncertain motion dynamics and imperfect observations. The state-space model and measurement model are introduced in the following paragraphs.

1) *State-Space Model*: The 2D motion of the BD in discrete time steps indexed by k is considered. Let $\mathbf{x}[k] = [p_x[k], v_x[k], p_y[k], v_y[k]]^T$ indicate the position of BD (p_x, p_y) and velocity (v_x, v_y) of the BD at time instance k . Then, a standard kinematic evolution model [46] in discrete time is implemented as follows:

$$\mathbf{x}[k+1] = \mathbf{F} \mathbf{x}[k] + \mathbf{G} \mathbf{w}[k], \quad (15)$$

where \mathbf{F} and \mathbf{G} are given by

$$\mathbf{F} = \begin{bmatrix} 1 & 0 & T_s & 0 \\ 0 & 1 & 0 & T_s \\ 0 & 0 & 1 & 0 \\ 0 & 0 & 0 & 1 \end{bmatrix}, \quad \mathbf{G} = \begin{bmatrix} \frac{1}{2}T_s^2 & 0 \\ 0 & \frac{1}{2}T_s^2 \\ T_s & 0 \\ 0 & T_s \end{bmatrix}, \quad (16)$$

respectively. The term $\mathbf{w}[k] \sim \mathcal{N}(\mathbf{0}, \mathbf{Q}_w)$ is zero-mean white Gaussian noise with $\mathbf{Q}_w = \sigma_w^2 \mathbf{I}$ capturing random accelerations, where \mathbf{I} denotes an identity matrix. Moreover, T_s is the sampling interval. In (16), the state transition matrix \mathbf{F} indicates the linearized 2D kinematic model. The model assumes that the state of the BD is perturbed by a random acceleration as moving, such that the white noise $\mathbf{w}[k]$ appropriately changes the state. The model has been widely utilized in kinematic system for tracking applications [46], known as the white-noise acceleration model.

2) *Measurement Model*: At each time instance k , the measurement vector can be expressed by

$$\mathbf{z}[k] = \{\mathcal{I}[k], \mathcal{R}_{\text{dB}}[k]\}, \quad (17)$$

consisting of a set of detected LED IDs denoted by $\mathcal{I}[k]$ and a measured RSS value denoted by $\mathcal{R}_{\text{dB}}[k]$ of the backscatter signal, which can be expressed by

$$\mathcal{R}_{\text{dB}}[k] = R_{\text{dB}}^{\text{BC}}(\mathbf{x}[k]) + v[k], \quad (18)$$

with $v[k] \sim \mathcal{N}(0, \sigma_v^2)$ denoting the measurement noise. The function $R_{\text{dB}}^{\text{BC}}(\cdot)$ is the RSS model of the backscatter signal described in (13) in logarithmic scale. The set $\mathcal{I}[k]$ includes all LED APs whose coverage regions contain the position of the BD; if none of LED APs illuminates the BD, the set is empty. We apply a match-or-penalty approach for comparing the

measured and predicted LED sets, and a Gaussian likelihood is applied for the RSS term with noise variance R_v . This leads to a joint measurement likelihood function that attains the form

$$p(\mathbf{z} | \mathbf{x}) \propto p(\mathcal{I}^{\text{mea}} | \mathcal{I}^{\text{pred}}) \times \exp\left(-\frac{(\mathcal{R}_{\text{dB}}^{\text{mea}} - \mathcal{R}_{\text{dB}}^{\text{pred}})^2}{2R_v}\right), \quad (19)$$

where \mathcal{I}^{mea} and $\mathcal{I}^{\text{pred}}$ represent the measured and predicted LED IDs, respectively. Similarly, $\mathcal{R}_{\text{dB}}^{\text{mea}}$ and $\mathcal{R}_{\text{dB}}^{\text{pred}}$ denotes the measured and predicted RSS of the backscatter signal, respectively. Moreover, $\mathcal{I}^{\text{pred}}$ is obtained by checking the IDs of the LED APs that fall inside the FoV of the BD-equipped photodetector at the position of $\mathbf{x}[k]$, referring a known VLC deployment with LED illumination map in the space of interest.

Algorithm 1: PF Tracking Algorithm Pseudo-code

Input: measurements $\mathbf{z}[k] = (\mathcal{I}^{\text{mea}}, \mathcal{R}_{\text{dB}}^{\text{mea}})$, process noise covariance \mathbf{Q}_w , measurement noise variance R_v
Output: State estimates $\hat{\mathbf{x}}[k]$

1 Initialization:
2 Generate N_p particles $\{\mathbf{x}_i[0]\}_{i=1}^{N_p} \sim \mathcal{N}(\mathbf{0}, \mathbf{Q}_0)$
3 Assign equal weights $w_i[0] = 1/N_p$ to all particles

4 Prediction:
5 **for** each particle $i = 1$ to N_p **do** // State evolution
6 | Sample process noise $\mathbf{w}_i[k] \sim \mathcal{N}(\mathbf{0}, \mathbf{Q}_w)$
7 | Predict particle state using (15)
8 **end**

9 Measurement Update:
10 **for** each particle $i = 1$ to N_p **do** // Weight computation
11 | Compute predictions: $(\mathcal{I}^{\text{pred}}, \mathcal{R}_{\text{dB}}^{\text{pred}})$ using $\mathbf{x}_i[k]$
12 | Compare with observations: $(\mathcal{I}^{\text{mea}}, \mathcal{R}_{\text{dB}}^{\text{mea}})$
13 | Evaluate:
14 | $w_i[k] = p(\mathcal{I}^{\text{mea}} | \mathcal{I}^{\text{pred}}) \times \exp\left(-\frac{(\mathcal{R}_{\text{dB}}^{\text{mea}} - \mathcal{R}_{\text{dB}}^{\text{pred}})^2}{2R_v}\right)$
15 | Normalize weights: $w_i[k] \leftarrow w_i[k] / \sum_{j=1}^{N_p} w_j[k]$
16 **end**

17 Resampling:
18 Draw N_p samples from $\{\mathbf{x}_i[k]\}_{i=1}^{N_p}$ by interpreting $w_i[k]$ as probability and replace the old samples

19 State Estimate:
20 Compute weighted average of particles as the estimated state using (22)

3) *Sequential Monte Carlo method*: A particle filtering-based approach [46] is adopted to combine the measurements of LED IDs and the RSS of the backscatter signal for recursively estimating the location of the BD over time. With the aid of the state-space model (15) and measurement model (17), positioning and tracking of the BD is defined as a state estimation problem. The PF employs the sequential Monte Carlo method [46], which approximates the posterior distribution of the state of the BD in each time instance k as

$$p(\mathbf{x}[k] | \mathbf{z}[1:k]) \propto p(\mathbf{z}[k] | \mathbf{x}[k]) p(\mathbf{x}[k] | \mathbf{z}[1:k-1]), \quad (20)$$

where $p(\mathbf{x}[k] | \mathbf{z}[1:k-1])$ is the prior state and $p(\mathbf{z}[k] | \mathbf{x}[k])$ is the likelihood function in (19). The PF tracks the BD by sequentially updating the state $\mathbf{x}[k]$ using the measurements $\mathbf{z}[1:k]$. The pseudo-code in Algorithm 1 describes the main loop, including prediction, measurement update, resampling,

and state estimation. The initial state $\mathbf{x}[0] \sim \mathcal{N}(0, \mathbf{Q}_0)$ is represented by the N_p particles distributed in the space, where all particles are assigned to an equal weight $w[0]$ with normalization. During the prediction step, the state of each particle is propagated according to (15). The measurement update then adjusts the weight of each particle based on how well the prediction agrees with measurements, expressed by

$$w_i^{N_p}[k] = w_i^{N_p}[k-1] p(\mathbf{z}[k] | \mathbf{x}[k]). \quad (21)$$

In particular, the set of predicted LED IDs $\mathcal{I}^{\text{pred}}$ is obtained by checking which LED APs cover the location of the particles. The observed LED ID set \mathcal{I}^{mea} is compared with the predicted set $\mathcal{I}^{\text{pred}}$, and a neutral weight one is assigned if at least one ID is matched; a penalty weight zero is assigned otherwise. The RSS measurement of the backscatter signal refines this process by penalizing large deviations between the measured RSS $\mathcal{R}_{\text{db}}^{\text{mea}}$ and predicted RSS $\mathcal{R}_{\text{db}}^{\text{pred}}$, thereby involving the backscatter channel condition into the likelihood calculation. A resampling step is performed to avoid the degeneracy problem discussed in [46]. The particles with low weights are replaced by those with stronger weights, which maintains particle diversity and prevents weight collapse. Finally, the position of the BD is estimated as the posterior mean of the state over all particles, with the aid of

$$\hat{\mathbf{x}}[k] = \sum_{i=1}^{N_p} w_i[k] \mathbf{x}_i[k]. \quad (22)$$

Above BD position tracking process is recursively executed over time to provide continuous state estimation, thereby facilitating effective positioning and tracking of the BD. This combination of proximity-based LED ID matching and RSS refinement provides a low-complexity solution for the positioning and tracking purposes. It ensures that proximity information in terms of multiple LED APs imposes coarse constraints on the location of the BD, while the RSS observation delivers continuous measurement that guides the estimation toward a more precise direction.

4) *Computational Complexity Analysis*: Let N_p be the number of particles, L the number of LED APs or VLC cells, and $d = 4$ the dimension of the state vector \mathbf{x} . The prediction step costs $O(N_p)$. The LED-ID coverage evaluation tests each particle against L VLC cells and therefore costs $O(N_p L)$ in the worst case, which dominates when $L \geq 2$. Furthermore, the RSS likelihood calculation, weight normalization, resampling, and posterior averaging require $O(N_p)$ for each step. Summing these contributions gives the per-step time complexity $\mathcal{C} = O(N_p L)$. Moreover, the working memory scales linearly with the number of particles, thereby yielding a complexity of $O(N_p d)$. We therefore consider time complexity as the primary metric of the algorithm, since $L > d$ applies to the most use case scenarios.

IV. IMPLEMENTATIONS

An experimental proof of concept is developed to validate the feasibility and effectiveness of the proposed system. Fig. 4 shows the experimental setup, and Table I summarizes the information of used electronic components and measurement

TABLE I
HARDWARE COMPONENTS OF IMPLEMENTATION

Parameter	Key Component	Model
LED AP	DC supply	Radionet PSU-3
	MCU (AC supply)	Raspberry Pi RP2040
	Driver chip	OnSemi CAT4109
	LED	OSRAM GW 19LHS2.4M
BD	PV cell	TDK BCS2717B6
	Comparator	TI TLV7031
	RF switch	Analog Devices ADG919
	Antenna	Omni-directional dipole
RFS	Signal generator	R&S SGT100A
	Antenna	Omni-directional dipole
Reader	SDR	NI USRP X300
	Antenna	Omni-directional dipole
	Laptop	Dell Latitude 7420

equipment. Experiments are performed in an indoor environment with a total of 6 LED luminaires mounted on the ceiling to provide illumination and proximity information. Each luminaire consists of 7 LEDs transmitting the same VLC signal, broadcasting its unique ID using the FDM method as discussed in Section III-C.

A. Hardware Design and Configuration

A Raspberry Pi RP2040 microcontroller unit (MCU) is used to generate the LED-modulating signals for the luminaires. These signals are generated using Manchester encoding and BFSK modulation. The frame structure of the modulating signal consists of preambles for signal detection and synchronization, followed by a payload for positioning that included an 8-bit LED ID and a dummy bit. The preamble is a 7-bit Barker sequence of '1110010' to enhance autocorrelation properties in detection. An LED driver module based on two OnSemi CAT4109 chips is then employed to bias the modulating signals with direct current from a constant DC power supply. The driver module is capable of driving the 6 LED luminaires simultaneously, each of them emitting their BFSK-modulated signal provided by a dedicated programmable input/output pin of the MCU. The BFSK modulation frequencies are chosen to be higher than 2 kHz to eliminate visible flicker in the emitted light. Referring the VLC deployment strategy discussed in Section III-C, a complete VLC cluster is formed by LED-1, LED-2, LED-3, and LED-4, with each using a distinct pair of BFSK frequencies $\{f_{i,1}, f_{i,2}\}$ for $i \in \{1, 2, 3, 4\}$. Another incomplete VLC cluster includes LED-5 and LED-6, which use the same frequency pairs as LED-1 and LED-3, respectively. The numerical value of used frequencies are listed in Table II. This design enables continuous broadcasting of the ID assigned to each luminaire via the VLC link. When the BD detects light from any luminaires, it reports the corresponding IDs, thereby indicating its proximity to the luminaires.

Fig. 5 shows the BD prototype with a circuit diagram. A PV cell TDK BCS2717B6 is employed to harvest light energy from the luminaires, converting the optical power into an electrical voltage V_{PV} . The voltage V_{PV} is fed into the positive input of a comparator Texas Instruments TLV7031 and an RC low-pass filter (LPF) consisting of a 100 k Ω resistor and a 0.1 μF capacitor with a 15 Hz cutoff frequency. The LPF output, denoted by V_{LPF} , provides the DC component of V_{PV} to the negative comparator input. When the instantaneous

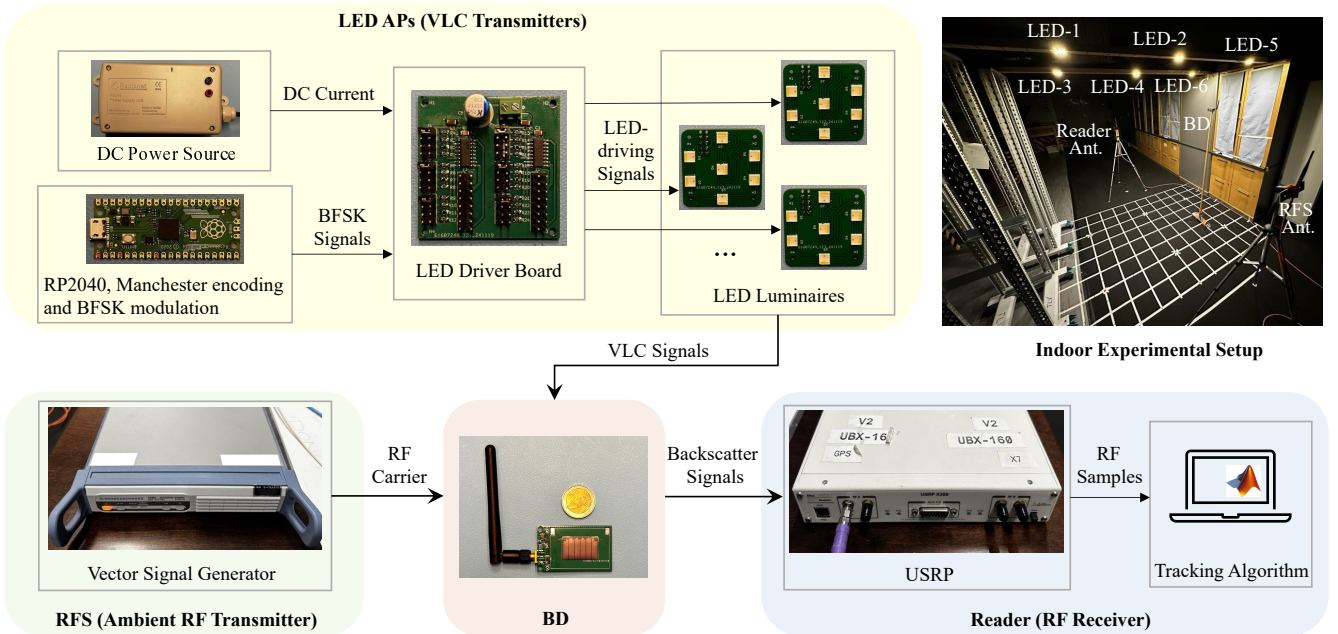


Fig. 4. Implementation of the proof of concept. Six LED luminaires emit VLC signals embedded with their IDs. A signal generator emits 2.4 GHz carrier waves. The BD receives the VLC signals, converts them into electrical signals and modulates with the carrier signal. The modulated signals are backscattered and captured by a USRP, which is connected to a host computer for signal processing and location inference of the BD. The setup is within an indoor space.

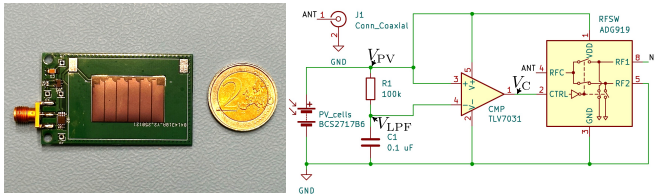


Fig. 5. Prototype of the BD with its schematic. A 2-euro coin is placed in the picture to show the scale of the BD prototype.

V_{PV} exceeds V_{LPF} , the comparator output V_C rises to the high binary level. Otherwise, V_C falls to the low binary level. The comparator output controls the RF switch Analog Devices ADG919 that modulates the incidence RF carrier waves captured by the dipole antenna. The termination of the antenna is alternated between two loads Z_1 and Z_2 . Assuming that the antenna is matched to a characteristic impedance $Z_a = 50 \Omega$, the complex reflection coefficient [41] takes the form $\Gamma_i = \frac{Z_i - Z_a^*}{Z_i + Z_a}$, and thus the modulation factor [41] is expressed by $M = \frac{1}{4} |\Gamma_1 - \Gamma_2|^2$. The maximum efficiency $M = 1$ can be achieved when $Z_1 = \infty$ and $Z_2 = 0$, corresponding to the switch either opening or shorting the antenna termination.

The BD harvests energy from visible light to power its circuitry, enabling energy-neutral operation. For instance, at an illuminance of 200 lx, the selected PV cell delivers an operating current of 10 μ A at 2.6 V, which corresponds to about 26 μ W of harvested electrical power. For the electronic components of the BD at the same supply voltage, the RF switch draws about 0.10 μ A in typical conditions (maximum 1.0 μ A), and the comparator draws about 0.315 μ A in typical conditions (maximum 0.90 μ A). These figures give a typical BD power of roughly 1.08 μ W and a maximum power of

roughly 4.94 μ W at 2.6 V. Thus, the output power from the PV cell comfortably exceeds the power consumption of the BD, thereby supporting energy-neutral operation of the device.

An RF signal generator Rohde & Schwarz SGT100A emits an unmodulated sine-wave carrier signal at $f_c = 2.4$ GHz, serving as the RFS. When the carrier signal arrives at the antenna, it gets mixed with the switch control signal V_{CTRL} by the switching operation. The modulated signal which carries the LED IDs is backscattered to the reader. The RF reader is composed of the National Instruments software-defined radio (SDR) USRP X300 that collects the RF samples at a sampling rate $f_s = 200$ kHz. The samples are conveyed to a host computer, which performs detection of the LED IDs, measures the RSS of backscatter signals, and executes the tracking algorithm described in Section III-D.

B. Signal Processing at Reader

The signal processing flow at the reader side is visualized in Fig. 6. The USRP-received RF samples centered at the carrier frequency f_c are first down-converted and then low-pass filtered, resulting in a stream of in-phase and quadrature (I/Q) samples at the reader side. These samples are quantized into complex values and transferred to a laptop running MATLAB R2024b for demodulation. A non-coherent FSK demodulator is designed to process the received samples [47]. After filtering out the high-frequency noise using an LPF with an approximate cut-off frequency $f_{cut} = 20$ kHz at 3 dB, a filter bank with four pairs of band-pass filters (BPFs) is applied to the incoming samples. Each pair of filters has a 10 dB bandwidth of approximately $f_\Delta = 500$ Hz and is allocated to a specific frequency pair of an LED AP, introduced in Section IV-A. The outputs of the two BPFs in each pair are envelope-detected and

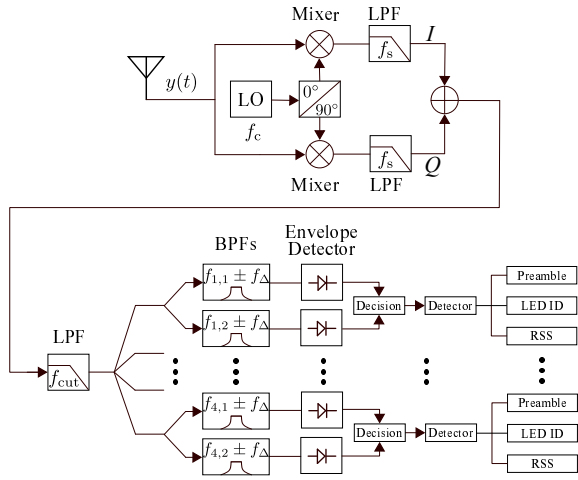


Fig. 6. Signal processing flow of the received backscatter signals at the reader.

compared to determine which one exhibits greater magnitude, thereby indicating the bit associated with that instant of time. The bit sequence produced by this comparison is then examined to detect a preamble, and the subsequent ID of the LED AP is extracted. The extracted ID is combined with the measured RSS to form the measurement vector in (17). These quantities are finally passed to the tracking algorithm described in Section III-D, where they serve as the measurement inputs for tracking the position of the BD.

This setup provided a practical implementation of the joint VLC-BC system for the tracking purpose, enabling the low-complexity and energy-neutral BD design to receive and forward the proximity information without an external power supply and active RF synthesizers. The setup is evaluated in an indoor environment. The experimental results are presented and discussed in Section V.

V. SIMULATION AND EXPERIMENTAL RESULTS

We conduct a series of simulations and experiments to evaluate the performance of the proposed indoor tracking system. This section presents the methodology and findings of both the simulations and the experimental validations.

A. Simulations

A rectangular space of dimensions $2.5 \times 2.5 \text{ m}^2$ is considered, with 6 LED APs mounted on the ceiling at a height of $h_{\text{LED}} = 1.9 \text{ m}$. The LED APs are arranged in a grid with spacing $d_{\text{LED}} = 0.8 \text{ m}$ to ensure dense illumination and coverage. All LED AP emit visible light at an optical power of 2.1 W , continuously and repeatedly transmitting packets via VLC signals using the discussed FDM method. Each packet consists of a unique 8-bit ID of the LED AP, preceded by a 7-bit Barker code preamble sequence for synchronization. An unmodulated sine-wave RF carrier at $f_c = 2.4 \text{ GHz}$ and a power of 20 dBm is generated by an omni-directional dipole antenna positioned at $(x, y, z) = (1.2, -0.5, 1.5) \text{ m}$, while an RF receiver with an omni-directional dipole antenna is placed at $(x, y, z) = (1.2, 2.0, 1.5) \text{ m}$ for sampling at a rate of 200 kSa/s . Received samples are then processed by the non-coherent FSK demodulator discussed in Section IV-B to

TABLE II
SIMULATION AND EXPERIMENTAL PARAMETERS

Parameter	Value	Description
$W \times L$	2.5×2.5	Size of the target area [m^2]
$h_{\text{LED}}, h_{\text{BD}}$	$2.0, 1.57$	Height of LED APs and BD [m]
$h_{\text{RFS}}, h_{\text{Reader}}$	$1.5, 1.5$	Height of RFS and Reader [m]
$(x, y)_{\text{RFS}}$	$(1.2, -0.5)$	2D position of RFS [m]
$(x, y)_{\text{Reader}}$	$(1.2, 2.0)$	2D position of reader [m]
$(x, y)_{\text{LED}}$	$(0.4, 1.2) (1.2, 0.4) (0.4, 1.2) (1.2, 1.2) (2.0, 0.4) (2.0, 1.2)$	2D positions of LED APs 1-6 [m]
A_{PD}	0.027×0.017	Active area of the BD-equipped PD (PV cell) [m^2]
Φ_{max}	60	LED radiation semi-angle at half power [deg]
Ψ	60	FoV semi-angle of the PD's light acceptance cone [deg]
$\eta_{\text{E-O}}$	2.1	LED power electric-optical conversion factor [W/A]
$\eta_{\text{O-E}}$	0.5	Responsivity of the BD-equipped PD [A/W]
B	50	System operational bandwidth [kHz]
ϵ	0.75	Fill factor
I_{Bias}	0.75	LED driving current [A]
I_0	10^{-9}	Dark saturation current [A]
V_t	25×10^{-3} (8.254, 9.004)	Thermal voltage [V]
$(f_{i,1}, f_{i,2})$	$(10.074, 10.990) (11.918, 13.002) (13.742, 14.992)$	Frequency pairs of light-modulating signal [kHz]
P_c	20	RFS carrier power [dBm]
f_c	2.4	RFS carrier frequency [GHz]
$G_{\text{T}}, G_{\text{R}}, G_{\text{BD}}$	3, 3, 1.5	Antenna gain of RFS, reader, and BD [dBi]
$\chi_{\text{f}}, \chi_{\text{b}}$	0.5, 0.5	Polarization mismatch
M	0.5	Modulation factor
Θ	0	On-object penalty
R	1 kbit/s	System data rate
N_0	-174	Noise power spectral density [dBm/Hz]
$(\sigma_{\text{LoS}}, \sigma_{\text{NLoS}})$	(3, 8.03)	Shadowing factors in the 3GPP model [dB]
N	5000	Number of particles
T_s	0.2	Sampling interval [s]
σ_v	5	Standard deviation of RSS measurement noise [dB]
σ_w	1	Standard deviation of process noise

extract LED IDs and measure the RSS of the backscatter signals. The decoded LED IDs and measured RSS values are then input to the tracking algorithm discussed in Section III-D for the estimation of the position of the BD. The main parameters used in the simulations to characterize the VLC link and BC link are summarized in Table II.

Since the size of the VLC cell affects the coverage where the BD can capture light and report its proximity, the aggregated VLC signal power received at the BD is simulated in the region of interest for different cell sizes. Different vertical distances between LED APs and the BD are considered to alternate the size of VLC cells. As an example, three vertical positions of the BD at 1.40, 1.57, and 1.70 m from the floor level are tested, considering that the heights of LED APs are fixed. As discussed in Section III-B, a lower height of BD yields a larger VLC cell coverage, whereas a higher height results in a smaller VLC cell size. Fig. 7 illustrates the resulting heatmaps of the VLC signal power arriving at the BD. Colors range from dark blue to bright yellow, corresponding to low through high power levels. Each LED AP is observed to illuminate an approximate circular area, referred to as a VLC cell. The overlapping areas of these circles indicate regions where the BD is able to simultaneously receive multiple VLC signals through the aforementioned FDM method. When the vertical position of the BD increases, the received VLC signal power from the nearest LED AP grows as well because of the shorter VLC link distance, whereas the coverage region shrinks and the overlapping zones between LED cells decrease.

Monte Carlo simulations are performed in MATLAB R2024b to evaluate the positioning functionality and accuracy. The positioning error is measured by root-mean-square error (RMSE) and mean absolute error (MAE) in terms of

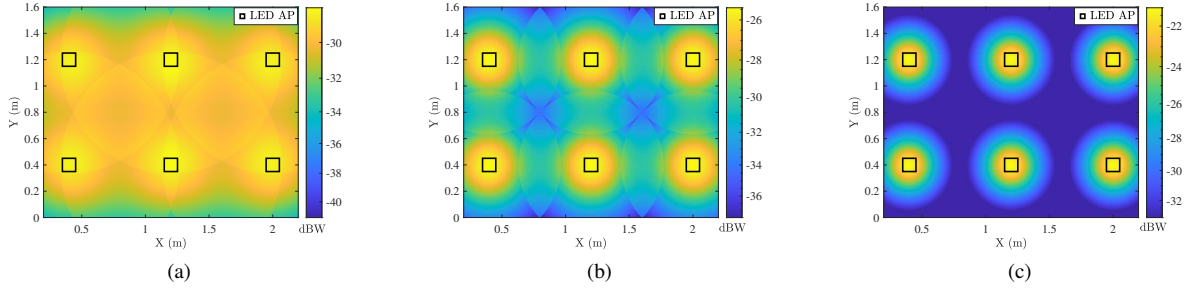


Fig. 7. Heatmap of the simulated VLC signal power at the BD over the space of interest. Colors range from dark blue to bright yellow, corresponding to low through high received power levels of the VLC signal. Different vertical distances between LED APs and the BD are demonstrated, yielding different size of VLC cells: (a) $h_{BD} = 1.40$ m ($r_{cell} = 0.87$ m), (b) $h_{BD} = 1.57$ m ($r_{cell} = 0.57$ m), (c) $h_{BD} = 1.70$ m ($r_{cell} = 0.35$ m).

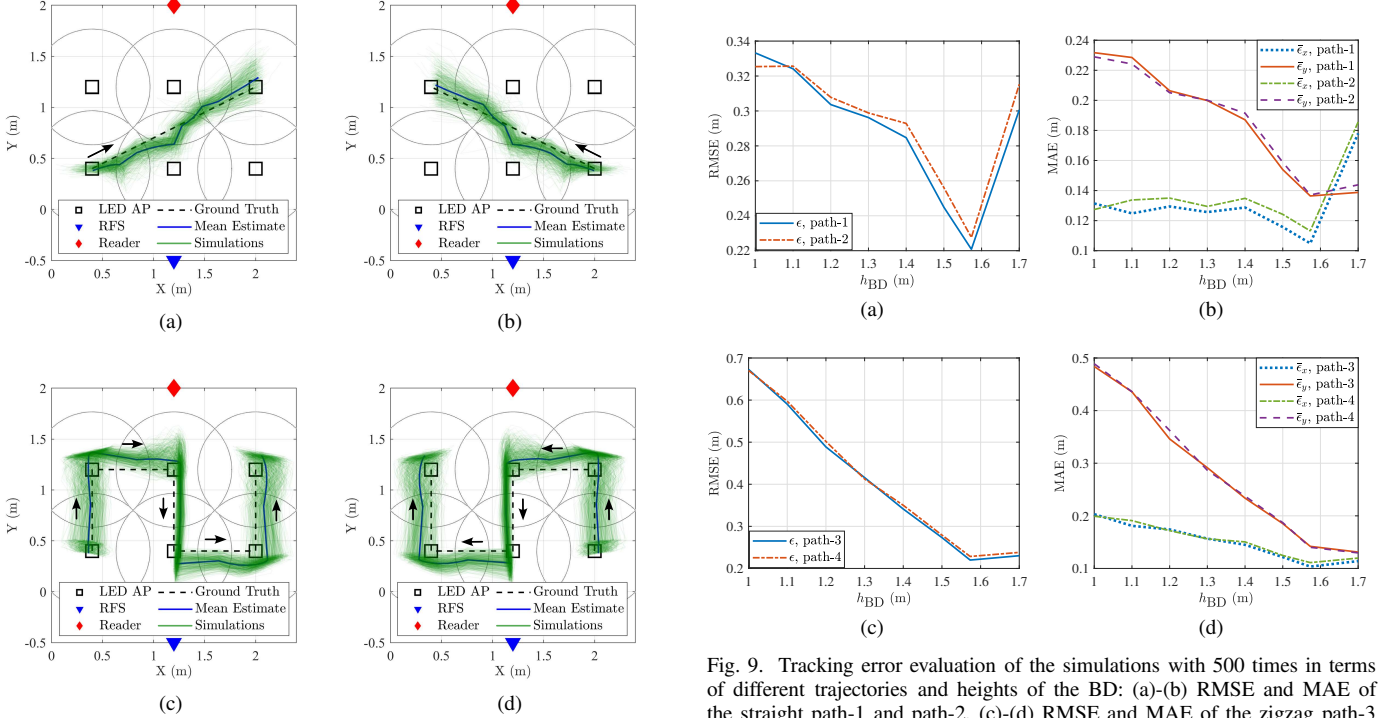


Fig. 8. Monte Carlo simulations of tracking experiment with 500 times for multiple trajectories: (a)-(b) path-1 and path-2 with straight-line shape, (c)-(d) path-3 and path-4 with zigzag shape. In each plot, the black dashed line is the ground truth of BD movement, the green lines show the repetitions of tracking simulation, and the blue solid line indicates the mean estimate. Arrows illustrate the directions of BD movement.

x -direction and y -direction. The RMSE is defined as

$$\epsilon = \sqrt{\frac{1}{K} \sum_{k=1}^K \|\mathbf{p}[k] - \hat{\mathbf{p}}[k]\|^2}, \quad (23)$$

where $\mathbf{p}[k] = (p_x[k], p_y[k])$ is the actual BD position at the time instance k , and $\hat{\mathbf{p}}[k] = (\hat{p}_x[k], \hat{p}_y[k])$ is the estimated position, and K is the total number of estimations. The MAE values in the x and y directions are given by

$$\bar{\epsilon}_x = \frac{1}{K} \sum_{k=1}^K |p_x[k] - \hat{p}_x[k]|, \quad \bar{\epsilon}_y = \frac{1}{K} \sum_{k=1}^K |p_y[k] - \hat{p}_y[k]|. \quad (24)$$

Four movement trajectories of the BD are simulated in the region, including two straight lines labeled by path-1 and path-2, and two zigzag routes labeled by path-3 and path-4, respectively. Each trajectory is designed to cross the VLC

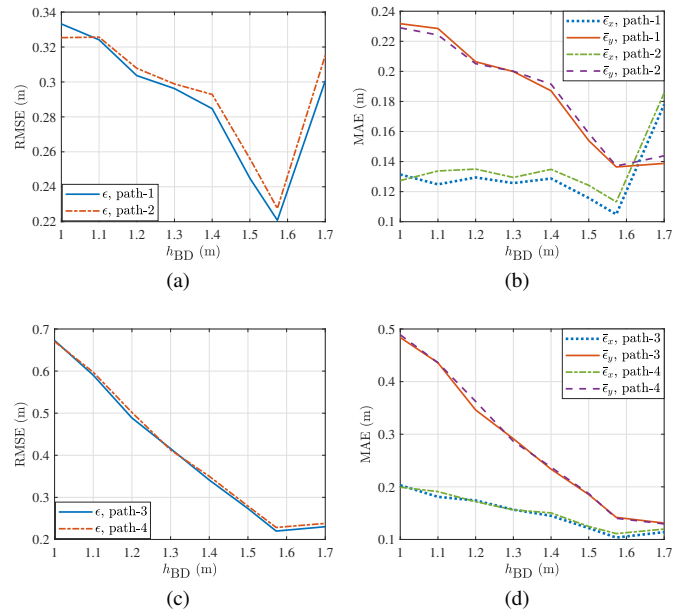


Fig. 9. Tracking error evaluation of the simulations with 500 times in terms of different trajectories and heights of the BD: (a)-(b) RMSE and MAE of the straight path-1 and path-2, (c)-(d) RMSE and MAE of the zigzag path-3 and path-4.

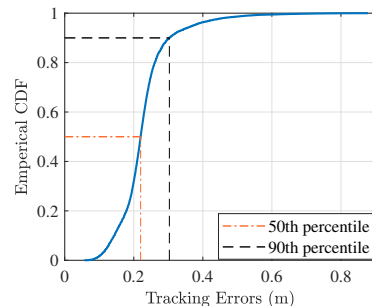


Fig. 10. Empirical CDF of the positioning errors among simulations carried out across all trajectories.

cells and their overlapping areas for a stress test of the tracking system. Since the height of LED APs is fixed in the experimental setup, various vertical positions of BD, ranging from 1.00 to 1.70 m, are simulated to examine the effect of the VLC cell size on the positioning performance. Each trajectory is simulated 500 times to collect comprehensive statistical data. As an example, Fig. 8 visualize the simulated BD tracking results of the four trajectories, respectively, with

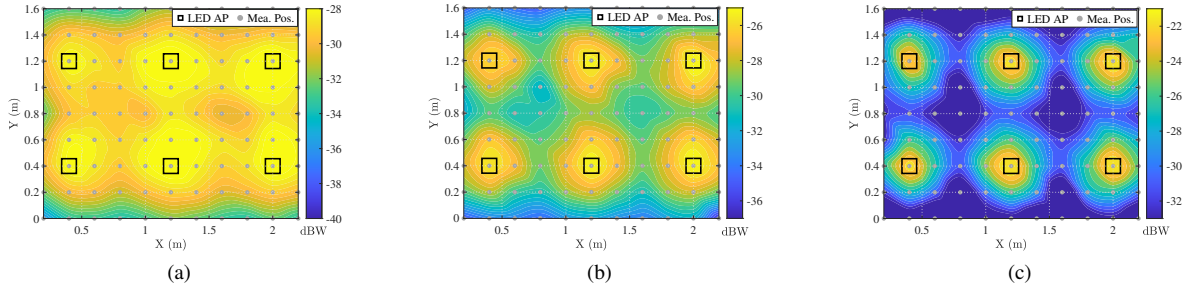


Fig. 11. Heatmap of the measured light intensity at the BD over the space of interest. Colors range from dark blue to bright yellow, corresponding to the power levels of the received VLC signal. Different vertical distances between LED APs and the BD are demonstrated, showing different pattern of the light reception: (a) $h_{BD} = 1.40$ m, (b) $h_{BD} = 1.57$ m, (c) $h_{BD} = 1.70$ m.

TABLE III
EXPERIMENTAL RESULTS

	Straight track			Zigzag track		
	Path 1	Path 2	Path 3	Path 4	Path 3	Path 4
RMSE (m)	$\bar{\epsilon}_x \pm \sigma_x$ (m)	$\bar{\epsilon}_y \pm \sigma_y$ (m)	RMSE (m)	$\bar{\epsilon}_x \pm \sigma_x$ (m)	$\bar{\epsilon}_y \pm \sigma_y$ (m)	RMSE (m)
Exp 1.	0.282	0.218 \pm 0.018	0.096 \pm 0.005	0.236	0.151 \pm 0.008	0.144 \pm 0.005
Exp 2.	0.278	0.220 \pm 0.012	0.115 \pm 0.004	0.242	0.181 \pm 0.009	0.106 \pm 0.006
Exp 3.	0.287	0.229 \pm 0.020	0.074 \pm 0.006	0.273	0.196 \pm 0.014	0.134 \pm 0.005
Exp 4.	0.241	0.189 \pm 0.014	0.065 \pm 0.005	0.257	0.148 \pm 0.016	0.145 \pm 0.008
Exp 5.	0.244	0.206 \pm 0.010	0.061 \pm 0.004	0.264	0.190 \pm 0.013	0.128 \pm 0.005

$h_{BD} = 1.57$ m. The green lines indicate estimated trajectories over all simulation repetitions, and the blue solid line shows the mean estimate. The arrows indicate the moving directions. It can be seen that the estimated trajectories closely follow the ground truth under the proposed algorithm. Fig. 9 presents the overall positioning performance in terms of different vertical positions of the BD with all trajectories. More specifically, Fig. 9(a) and Fig. 9(b) display the RMSE and MAE for the two straight paths, whereas Fig. 9(c) and Fig. 9(d) display the results for the two zigzag paths.

The results indicate that, when the vertical distance between the LED APs and the BD decreases with the incremental h_{BD} , the RMSE and MAE first decrease and then increase. An exemplary best performance is observed around $h_{BD} = 1.57$ m, achieving RMSE values of about 0.227, 0.228, 0.220, and 0.228 m for the four paths, respectively. The improvement at moderate heights comes from stronger LoS reception to the nearest LED AP, though if the BD is placed too high, overlapping regions between VLC cells diminish, creating outage zones where no VLC signal is received, as shown in Fig. 7. Moreover, the effect on the y -axis error is found to be more pronounced than that on the x -axis error. Fig. 10 shows the empirical cumulative distribution function (CDF) of tracking errors across all trajectories, indicating a median error of 0.220 m and 90th-percentile error of 0.303 m, with errors ranging from 0.058 m to 0.878 m.

B. Proof-of-Concept Experiments

Proof-of-concept experiments are conducted in an indoor room with parameters consistent with those used in the simulations. Fig. 4 illustrates the hardware configuration with details discussed in Section IV. Light intensity measurements are conducted to confirm the illumination coverage in the region and to validate the simulation result presented in Fig. 7. A light meter is placed at 99 positions on a 0.2 m grid, which are marked with gray dots in Fig. 11. The light intensity is measured at three different vertical positions of the BD to

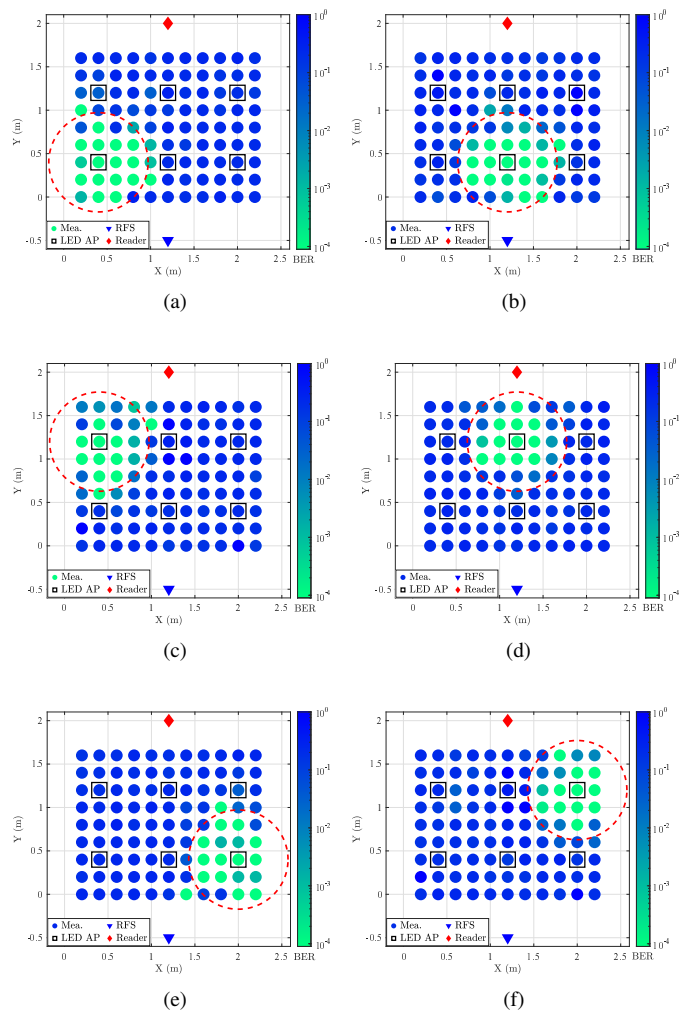


Fig. 12. Spatial distribution of end-to-end communication BER measurement: (a)-(f) The decoded LED ID originated from LED-1 through LED-6. The red dashed circles indicating the estimated coverage range of the VLC cell with a radius $r_{cell} = 0.572$ m calculated by (14). Lower BER values denoted by lighter colored positions are observed inside the corresponding VLC cell, indicating that the BD receives and forwards the LED ID belongs to that cell.

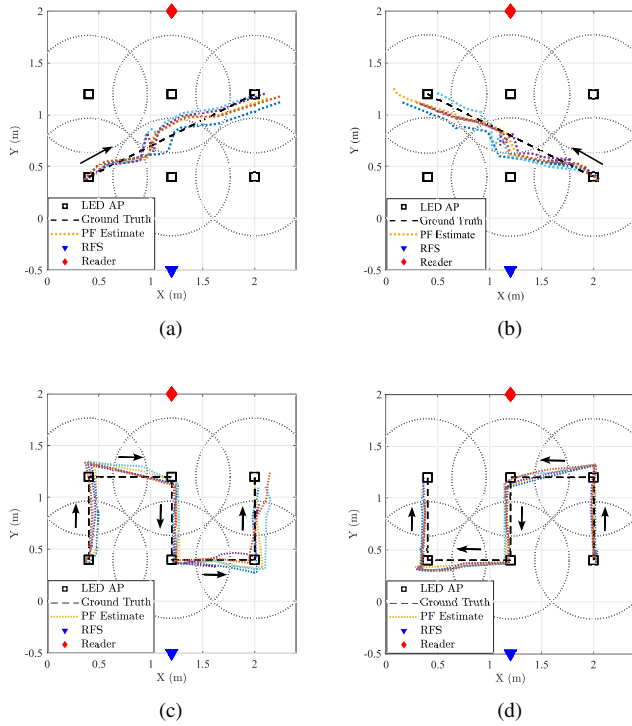


Fig. 13. Experimental results of tracking the BD on path 1-4 with 5 repetitions. The black dashed line is the ground truth of movement, the dotted lines are the estimated trajectories, and the arrow indicates the movement direction.

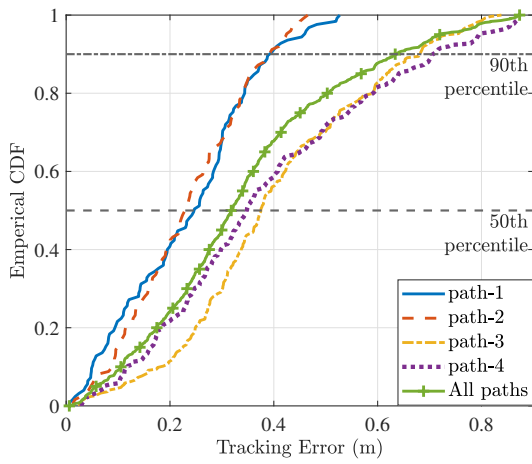


Fig. 14. Empirical CDF of the positioning errors among measurements carried out across all trajectories. For all tested paths, a median error of 0.318 m and a 90th-percentile error of 0.634 m are observed.

keep consistency with the simulations. Fig. 11 visualizes the measured power heatmaps after interpolation. It can be found that the spatial distribution of the received light power closely matched the simulated VLC cell coverage patterns in Fig. 7, including the approximately circular illumination zones and dark regions indicating potential outages where the BD cannot receive sufficient VLC signals and forward its proximity.

To further verify the effective VLC reception region of the BD in terms of each LED AP, end-to-end communication bit-error-rate (BER) measurements are conducted. The BD is placed at the same 99 positions on a 0.2 m grid in the

space at a height of 1.57 m, where the reader USRP performs sampling for 110 seconds in each marked position. The recorded samples are processed with the workflow discussed in Section IV-B, where the BER is then calculated. Fig. 12(a)-Fig. 12(f) show the spatial BER measurement results for the decoded LED ID originated from LED-1 through LED-6, superimposed with red circles indicating the theoretical VLC cell with a radius $r_{\text{cell}} = 0.572$ m calculated by (14). Low BER values below 10^{-3} are observed inside the corresponding VLC cell, indicating that the BD is able to receive and forward the LED IDs belongs to that cell. The overall results confirm successful communications between LED APs, the BD, the RFS, and the reader, allowing the BD to report its proximity within each relevant VLC cell.

To validate the tracking functionality of the proposed system, four BD movement trajectories identical to those used in the simulations are tested to assess positioning performance. The BD is affixed to a stand at a height of 1.57 m, which is moved along the trajectories at approximately 0.36 m/s for the straight-line paths and 0.40 m/s for the zigzag paths. The experiment on each path is repeated five times. During the experiment, a researcher carefully moves the BD maintaining a bent posture to avoid blocking the light, with the near-constant gait speed following a metronome. The position of the BD is estimated on the laptop connected to the USRP, which continuously samples and processes the received signals using the methodology discussed in Section IV-B and the tracking algorithm discussed in Section III-D.

Fig. 13 presents the tracking results of all tested trajectories, where Fig. 14 shows the empirical CDF of positioning errors. The numerical results are summarized in Table III. For the straight-line paths, an average RMSE of 0.266 m is achieved for path-1, with a median error of 0.247 m and 90th-percentile error of 0.396 m. Similarly, for path-2, an average RMSE of 0.254 m is achieved, with a median error of 0.230 m and 90th-percentile error of 0.393 m. Furthermore, for the zigzag paths, an average RMSE of 0.442 m is achieved for path-3, with a median error of 0.375 m and 90th-percentile error of 0.682 m. Similarly, for path-4, an average RMSE of 0.442 m is obtained, with a median error of 0.349 m and 90th-percentile error of 0.709 m. Positioning errors of more complicated movements on path-3 and path-4 are observed to be larger than the errors of movements on path-1 and path-2. This performance gap is likely due to the near-constant velocity motion model implemented by the PF, which is well-suited for straight-line movement, whereas the frequent heading changes characteristic of zigzag trajectories introduce greater uncertainty and intensify particle impoverishment. Finally, across all the tested paths, a median positioning error of 0.318 m and a 90th-percentile error of 0.634 m are observed. The presented results demonstrate that submeter-level positioning accuracy is attainable with the proposed joint VLC-BC system, enabled by the low-complexity and batteryless BD.

C. Comparison with State-of-the-Art Systems

For comparison purpose, Table IV contrasts our joint VLC-BC design against representative indoor VLP baselines in

TABLE IV
COMPARISON WITH STATE-OF-THE-ART VLP SYSTEMS

System	Technique	Positioning Method	Device Power Supply	Hardware Complexity	Device Cost	Accuracy
[48]	VLC (camera)	Image features	Battery	High	High	0.05 m (50%), 0.1 m (90%)
[49]	VLC (camera) + IMU	Proximity + RSS trilateration	Battery	High	High	0.4 m (50%), 0.8 m (90%)
[23]	VLC (camera)	Proximity	DC power supply	High	High	Approx. 0.35 m
[18]	VLC (APD)	Phase	Raspberry Pi	High	High	0.043 m (50%), 0.098 m (90%)
[22]	VLC (PD)	Proximity	Arduino	Medium	Medium	Approx. 1.5 m
[50]	VLC (PD) + Bluetooth	Proximity + RSS trilateration	Battery	High	High	0.03-0.52 m
This work	VLC (PV cell) + BC	Proximity + RSS model	Energy harvesting	Low	Low	0.318 m (50%), 0.634 m (90%)

terms of technology, positioning method, device power supply, hardware complexity, device cost, and achieved accuracy. Two trends emerge in the surveyed systems. First, camera- and advanced photodetector-based designs can achieve centimeter-level to decimeter-level accuracy, whereas they depend on power-intensive photonic front ends and substantial on-board signal processing, resulting in the higher entries for complexity and cost of the device [18], [23], [48], [49]. Furthermore, they rely on battery- or DC-powered computing platforms, such as smartphones or microcontrollers. Second, proximity-based VLP schemes employ low-complexity photodetectors, such as photodiodes and PV cells for LED identity information reception, thereby reducing the device complexity. Nevertheless, they typically yields decimeter-level to meter-level resolution that limits fine-grained tracking [22]. Moreover, hybrid VLC-Bluetooth approach narrows this gap by combining VLC proximity with Bluetooth RSS trilateration for localization, yet it still inherit the energy and cost footprint of an active radio front end, such as a smartphone [50].

Our design follows a different division of labor: VLC is solely used for low-overhead LED identification indicating the proximity of the device, while the RSS of BC signal is adopted to refine the position estimation. Moreover, the device relies on BC for reporting the proximity to a reader, without requiring active, energy-intensive RF components on the device. This architecture eliminates sophisticated photonic front ends and avoids heavy on-device computation. Our designed battery-less BD has μ W-level power consumption, low hardware complexity, and low device cost, while sustaining submeter-level positioning accuracy. By concentrating data fusion and location estimation at the reader side, the device burden remains minimal. Consequently, the proposed VLC-BC solution offers a favorable accuracy-power-cost trade-off relative to the baseline systems, as reflected in Table IV.

Key Takeaways: While camera- and advanced PD-based VLP systems are appealing for higher-precision localization, their power and hardware demands make them not suited for large-scale and battery-free development of asset tracking implementations. By contrast, the proposed VLC-BC system preserves the energy-neutral, low-profile form factor without sacrificing practical accuracy, providing a feasible operating point for asset tracking where the cost of development and maintenance dominate the design space.

VI. CONCLUSION

In this paper, we have presented a joint VLC-BC system for indoor asset tracking. We have designed a low-complexity and energy-neutral BD to harvest light energy from LED APs and

forward its proximity by modulating and reflecting ambient RF carriers. We have also proposed a multi-cell VLC architecture leveraging on FDM method to assign distinct frequency pairs to adjacent cells, mitigating interference and providing reliable indoor lighting coverage. We have developed a lightweight PF-based algorithm at the edge RF reader to merge proximity reports and the RSS of backscatter signals for tracking the BD in real time. Simulations and experiments have verified that submeter-level tracking accuracy is achieved, despite the BD having low hardware complexity and non-active RF synthesizers. Compared with state-of-the-art VLP systems, our design has shown an accuracy-power-cost trade-off. By co-designing communication and computation between LEDs, BDs and the edge reader, this work offers a sustainable path to cost-effective, energy-neutral indoor localization in mobile and pervasive IoT deployments.

REFERENCES

- [1] O. López, R. K. Singh, D.-T. Phan-Huy, E. Katranaras, N. Mazloum, K. Ruttik, R. Jäntti, H. Khan, O. Rosabal, P. Alexias, P. Raghuvanshi, D. Ruiz-Guirola, B. Singh, A. Höglund, D. P. Van, A. Azarbahram, and J. Famaey, “Zero-energy devices for 6G: Technical enablers at a glance,” *IEEE Internet Things Mag.*, vol. 8, no. 3, pp. 14–22, Apr. 2025.
- [2] W. Saad, M. Bennis, and M. Chen, “A vision of 6G wireless systems: Applications, trends, technologies, and open research problems,” *IEEE Network*, vol. 34, no. 3, pp. 134–142, May 2020.
- [3] P. S. Farahsari, A. Farahzadi, J. Rezazadeh, and A. Bagheri, “A survey on indoor positioning systems for IoT-based applications,” *IEEE Internet Things J.*, vol. 9, no. 10, pp. 7680–7699, May 2022.
- [4] 3GPP, “Study on Ambient IoT in RAN,” 3GPP, Tech. Rep. TS 38.848, Jun. 2023, Ver. 18.0.0.
- [5] M. M. Butt, N. R. Mangalvedhe, N. K. Pratas, J. Harrebek, J. Kimionis, M. Tayyab, O.-E. Barbu, R. Ratasuk, and B. Vejlgaard, “Ambient IoT: A missing link in 3GPP IoT devices landscape,” *IEEE Internet Things Mag.*, vol. 7, no. 2, pp. 85–92, Mar. 2024.
- [6] A. Grenier, E. S. Lohan, A. Ometov, and J. Nurmi, “A survey on low-power GNSS,” *IEEE Commun. Surv. Tutor.*, vol. 25, no. 3, pp. 1482–1509, Apr. 2023.
- [7] C. Wu, F. Zhang, B. Wang, and K. J. R. Liu, “Easitrack: Decimeter-level indoor tracking with graph-based particle filtering,” *IEEE Internet Things J.*, vol. 7, no. 3, pp. 2397–2411, Mar. 2020.
- [8] R. Faragher and R. Harle, “Location fingerprinting with bluetooth low energy beacons,” *IEEE J. Sel. Areas Commun.*, vol. 33, no. 11, pp. 2418–2428, Nov. 2015.
- [9] K. Hu, C. Gu, and J. Chen, “LTrack: A LoRa-based indoor tracking system for mobile robots,” *IEEE Trans. Vehic. Technol.*, vol. 71, no. 4, pp. 4264–4276, Apr. 2022.
- [10] X. Zhou, L. Chen, Y. Ruan, and R. Chen, “Indoor localization with multi-beam of 5G new radio signals,” *IEEE Trans. Wireless Commun.*, vol. 23, no. 9, pp. 11 260–11 275, Sep. 2024.
- [11] J. Xu, Z. Li, K. Zhang, J. Yang, N. Gao, Z. Zhang, and Z. Meng, “The principle, methods and recent progress in RFID positioning techniques: A review,” *IEEE J. Radio Freq. Identif.*, vol. 7, pp. 50–63, Jan. 2023.
- [12] Z. Guo, D. Wang, L. Gui, B. Sheng, H. Cai, F. Xiao, and J. Han, “UWTracking: Passive human tracking under LOS/NLOS scenarios using IR-UWB radar,” *IEEE Trans. Mobile Comput.*, vol. 23, no. 12, pp. 11 853–11 870, Dec. 2024.

- [13] I. Demirkol, D. Camps-Mur, J. Paradells, M. Combalia, W. Popoola, and H. Haas, "Powering the Internet of Things through light communication," *IEEE Commun. Mag.*, vol. 57, no. 6, pp. 107–113, Jun. 2019.
- [14] Y. Zhuang, L. Hua, L. Qi, J. Yang, P. Cao, Y. Cao, Y. Wu, J. Thompson, and H. Haas, "A survey of positioning systems using visible LED lights," *IEEE Commun. Surv. Tuts.*, vol. 20, no. 3, pp. 1963–1988, Q3 2018.
- [15] Z. Zhu, Y. Yang, M. Chen, C. Guo, J. Cheng, and S. Cui, "A survey on indoor visible light positioning systems: Fundamentals, applications, and challenges," *IEEE Commun. Surv. Tuts.*, vol. 27, no. 3, pp. 1656–1686, Jun. 2025.
- [16] S. Bastiaens, M. Alijani, W. Joseph, and D. Plets, "Visible light positioning as a next-generation indoor positioning technology: A tutorial," *IEEE Commun. Surv. Tuts.*, vol. 26, no. 4, pp. 2867–2913, Q4 2024.
- [17] H. Yang, W.-D. Zhong, C. Chen, and A. Alphones, "Integration of visible light communication and positioning within 5G networks for Internet of Things," *IEEE Network*, vol. 34, no. 5, pp. 134–140, Sep. 2020.
- [18] H. Yang, S. Zhang, A. Alphones, C. Chen, K.-Y. Lam, Z. Xiong, L. Xiao, and Y. Zhang, "An advanced integrated visible light communication and localization system," *IEEE Trans. Commun.*, vol. 71, no. 12, pp. 7149–7162, Dec. 2023.
- [19] H. Yang, W.-D. Zhong, C. Chen, A. Alphones, P. Du, S. Zhang, and X. Xie, "Coordinated resource allocation-based integrated visible light communication and positioning systems for indoor IoT," *IEEE Trans. Wireless Commun.*, vol. 19, no. 7, pp. 4671–4684, Jul. 2020.
- [20] H. Yang, W.-D. Zhong, C. Chen, A. Alphones, and P. Du, "Qos-driven optimized design-based integrated visible light communication and positioning for indoor IoT networks," *IEEE Internet Things J.*, vol. 7, no. 1, pp. 269–283, Jan. 2020.
- [21] G. del Campo-Jimenez, J. M. Perandones, and F. J. Lopez-Hernandez, "A VLC-based beacon location system for mobile applications," in *Proc. IEEE Int. Conf. Localization GNSS*, Aug. 2013.
- [22] P. Cherntanomwong and W. Chantharasena, "Indoor localization system using visible light communication," in *Proc. IEEE Int. Conf. Inf. Technol. Electr. Eng.*, Chiang Mai, Thailand, Feb. 2015, pp. 480–483.
- [23] C. Xie, W. Guan, Y. Wu, L. Fang, and Y. Cai, "The LED-ID detection and recognition method based on visible light positioning using proximity method," *IEEE Photonics J.*, vol. 10, no. 2, pp. 1–16, Apr. 2018.
- [24] F. Wang, F. Yang, J. Song, and Z. Han, "Access frameworks and application scenarios for hybrid VLC and RF systems: State of the art, challenges, and trends," *IEEE Commun. Mag.*, vol. 60, no. 3, pp. 55–61, Mar. 2022.
- [25] H. Abuella, M. Elamassie, M. Uysal, Z. Xu, E. Serpedin, K. A. Qaraqe, and S. Ekin, "Hybrid RF/VLC systems: A comprehensive survey on network topologies, performance analyses, applications, and future directions," *IEEE Access*, vol. 9, pp. 160 402–160 436, Nov. 2021.
- [26] Y. Guo, K. Xiong, Y. Lu, D. Wang, P. Fan, and K. B. Letaief, "Achievable information rate in hybrid VLC-RF networks with lighting energy harvesting," *IEEE Trans. Commun.*, vol. 69, no. 10, pp. 6852–6864, Oct. 2021.
- [27] H. Peng, Q. Li, A. Pandharipande, X. Ge, and J. Zhang, "End-to-end performance optimization of a dual-hop hybrid VLC/RF IoT system based on SLIPT," *IEEE Internet Things J.*, vol. 8, no. 24, pp. 17356–17371, Dec. 2021.
- [28] P. D. Diamantoulakis, G. K. Karagiannidis, and Z. Ding, "Simultaneous lightwave information and power transfer (SLIPT)," *IEEE Trans. Green Commun. Netw.*, vol. 2, no. 3, pp. 764–773, Sep. 2018.
- [29] Y. Xiao, P. D. Diamantoulakis, Z. Fang, L. Hao, Z. Ma, and G. K. Karagiannidis, "Cooperative hybrid VLC/RF systems with SLIPT," *IEEE Trans. Commun.*, vol. 69, no. 4, pp. 2532–2545, Jan. 2021.
- [30] T. Tang, L. Shi, Q. Li, and Z. Xiong, "Sustainability-driven resource allocation for slant-assisted hybrid VLC/RF IoT systems," *IEEE Wireless Commun. Lett.*, vol. 13, no. 6, pp. 1765–1769, Jun. 2024.
- [31] V. Liu, A. Parks, V. Talla, S. Gollakota, D. Wetherall, and J. R. Smith, "Ambient backscatter: Wireless communication out of thin air," *ACM Comput. Commun. Rev.*, vol. 43, no. 4, pp. 39–50, Aug. 2013.
- [32] N. Van Huynh, D. T. Hoang, X. Lu, D. Niyato, P. Wang, and D. I. Kim, "Ambient backscatter communications: A contemporary survey," *IEEE Commun. Surv. Tutor.*, vol. 20, no. 4, pp. 2889–2922, May 2018.
- [33] T. Jiang, Y. Zhang, W. Ma, M. Peng, Y. Peng, M. Feng, and G. Liu, "Backscatter communication meets practical battery-free Internet of Things: A survey and outlook," *IEEE Commun. Surv. Tuts.*, vol. 25, no. 3, pp. 2021–2051, May 2023.
- [34] D. Giustiniano, A. Varshney, and T. Voigt, "Connecting battery-free IoT tags using LED bulbs," in *Proc. ACM Workshop on Hot Topics in Networks*, New York, NY, Nov. 2018, p. 99–105.
- [35] M. S. Mir, W. Yan, P. Dutta, D. Giustiniano, and A. Varshney, "Tunnel-LiFi: Bringing LiFi to commodity Internet of Things devices," in *Proc. Int. Workshop on Mobile Computing Systems and Applications*, New York, NY, Feb. 2023, p. 1–7.
- [36] M. S. Mir, B. G. Guzman, A. Varshney, and D. Giustiniano, "LiFi for low-power and long-range RF backscatter," *IEEE/ACM Trans. Netw.*, vol. 32, no. 3, pp. 2237–2252, Dec. 2023.
- [37] B. Xie, A. Dowhuszko, K. Koskinen, L. Mela, J. Lietzén, K. Ruttik, R. Jäntti, and J. Hämäläinen, "Integration of visible light and backscatter communications for ambient Internet of Things," in *Proc. IEEE Veh. Technol. Conf.*, Singapore, Singapore, Sep. 2024.
- [38] B. Xie, L. Mela, J. Lietzén, K. Ruttik, A. Dowhuszko, and R. Jäntti, "Light-controlled thin film backscatter device using additive manufacturing," *IEEE Sens. Lett.*, vol. 8, no. 5, pp. 1–4, May 2024.
- [39] K. Koskinen, B. Xie, K. Ruttik, and R. Jäntti, "Li2BC: From visible light communication to ambient RF backscatter," in *Proc. 16th Ger. Microw. Conf.*, Dresden, Germany, Mar. 2025, pp. 346–349.
- [40] M. Abedi, A. A. Dowhuszko, and R. Wichman, "Indoor planning of optical wireless networks for line-of-sight condition in access and backhauling," *IEEE Trans. Commun.*, vol. 73, no. 4, pp. 2538–2553, Sep. 2024.
- [41] J. D. Griffin and G. D. Durgin, "Complete link budgets for backscatter-radio and RFID systems," *IEEE Antennas Propag. Mag.*, vol. 51, no. 2, pp. 11–25, Jul. 2009.
- [42] 3GPP, "Study on channel model for frequencies from 0.5 to 100 GHz," 3GPP, Tech. Rep. TS 38.901, Jun. 2024, Ver. 18.0.0.
- [43] A. H. F. Raouf, C. K. Anjumappa, and I. Guvenc, "Optimizing energy-harvesting hybrid VLC/RF networks with random receiver orientation," *IEEE Access*, vol. 12, pp. 147 574–147 588, Oct. 2024.
- [44] N. Robertson, D. Sanders, P. Seymour, and R. Thomas, "The four-colour theorem," *Journal of combinatorial theory, Series B*, vol. 70, no. 1, pp. 2–44, May 1997.
- [45] D. Tse and P. Viswanath, *Fundamentals of Wireless Communication*. Cambridge University Press, 2005.
- [46] Y. Bar-Shalom, X. R. Li, and T. Kirubarajan, *Estimation with Applications to Tracking and Navigation: Theory Algorithms and Software*. John Wiley & Sons, 2004.
- [47] A. Goldsmith, *Wireless Communications*. Cambridge University Press, 2005.
- [48] Z. Zhu, R. Bao, Y. Yang, C. Guo, M. Chen, and W. Saad, "Positioning using visible light communications: A perspective arcs approach," *IEEE Trans. Wirel. Commun.*, Oct. 2023.
- [49] L. Li, P. Hu, C. Peng, G. Shen, and F. Zhao, "Epsilon: A visible light based positioning system," in *Proc. USENIX Symp. Netw. Syst. Des. Implement.*, Seattle, US, Apr. 2014, pp. 331–343.
- [50] L. Albraheem and S. Alawad, "A hybrid indoor positioning system based on visible light communication and bluetooth RSS trilateration," *Sensors*, vol. 23, no. 16, Jul. 2023.